Solar Energy Materials & Solar Cells 299 (2026) 114195

Contents lists available at ScienceDirect

Solar Energy Materials and Solar Cells

journal homepage: www.elsevier.com/locate/solmat

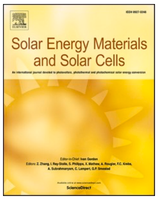

A novel damp heat-induced failure mechanism in PV modules (with case study in TOPCon)

Haoran Wang [a], Chandany Sen [a,*], Muhammad Umair Khan [a], Ting Huang [b], Hao Song [b], Munan Gao [b], Ruirui Lv [b], Yuanjie Yu [b], Bram Hoex [a,**]

[a] School of Photovoltaic and Renewable Energy Engineering, University of New South Wales, Sydney, NSW, 2053, Australia
[b] CSI Solar Co Ltd., Jiangsu, 215129, China

ABSTRACT

Silicon solar technology continues to dominate the market, with Tunnel Oxide Passivated Contact (TOPCon) technology leading in efficiency. However, as devices approach fundamental performance limits, new failure modes may emerge or existing ones may become more critical, and their long-term reliability remains insufficiently understood. This study investigates the effect of damp heat (DH) exposure on bifacial n-type TOPCon modules with laser-assisted fired contacts, utilising different encapsulants: EVA, POE, and EVA-POE-EVA (EPE). After 2000 h of DH testing, modules showed P_{max} losses ranging from ~6%$_{rel}$ to ~16%$_{rel}$, primarily due to reduced V_{oc} caused by increased rear-side recombination. Modules encapsulated with POE on both sides degraded least (~8%$_{rel}$), while those using white EVA on the rear side suffered higher losses, especially when combined with EPE on the front (~16%$_{rel}$). Material analyses revealed a degradation pathway driven by magnesium (Mg) additives in the white EVA. Under DH exposure, Mg hydrates and generates an alkaline micro-environment that corrodes the SiN_x:H layer, facilitating moisture ingress in the poly-Si and SiO_x layers. This enhances interfacial hydrogen concentration, leading to depassivation and Mg-rich shunting defects, thereby increasing $J_{0,\ rear}$ and reducing V_{oc}. These findings underscore the need to control encapsulant composition by limiting Mg in white EVA and improving cell passivation. The minimodules studied here were specifically fabricated R&D purposes to probe humidity-induced degradation pathways. Through an in-depth understanding of this mechanism and thorough optimisation of cell and encapsulant design, effective mitigation strategies have been integrated upstream of module production, substantially eliminating the risk in commercial modules.

1. Introduction

Silicon photovoltaic (PV) technology continues to dominate the global market, with tunnel oxide passivated contact (TOPCon) solar cells currently offering the highest efficiencies at comparatively low manufacturing costs [1]. Apart from the efficiency of solar cells, however, long-term reliability is also critical to achieve a low levelized cost of electricity (LCOE) [2]. Despite the advantages, TOPCon modules still encounter notable reliability challenges under high-humidity conditions, particularly in glass/backsheet configurations, which can result in significant power degradation [3–7]. Earlier studies have shown that encapsulation materials with high water vapour transmission rates (WVTR), including ethylene vinyl acetate (EVA) and certain polymer backsheets, are primary pathways for moisture ingress, which subsequently accelerates degradation processes within the module [3,4,8,9]. EVA has dominated as encapsulant in the module market in the past decade, but it can produce acetic acid through hydrolysis, which can result in discolouring, delamination, and metallisation corrosion [10–13]. To address these issues, encapsulants with low WVTRs, such as polyolefin elastomers (POE), as well as double-glass module designs, have been widely adopted to enhance the durability and reliability of PV modules [7]. These approaches can significantly limit, or in some cases nearly eliminate, moisture ingress into the module structure. POE encapsulants, as an EVA alternative, offer advantages such as strong PID resistance, high resistivity, and beneficial for modules deployed in harsh environmental conditions [14]. However, it is susceptible to issues like additive migration and delamination [15]. To balance reliability with manufacturing efficiency, a three-layer EVA–POE–EVA (EPE) film was developed, in which the POE core acts as a moisture barrier while the EVA outer layers ensure firm adhesion to cells and other module components [15,16]. Given the higher cost, weight, and breakage risk of double-glass modules [17,18], and the greater expense of low-WVTR encapsulants [7], the industry largely favours cost-effective glass/backsheet modules with EVA encapsulation. However, this approach remains economically and technically viable only if such modules can adequately mitigate performance losses associated with humidity

---

* Corresponding author.
** Corresponding author.
E-mail address: b.hoex@unsw.edu.au (B. Hoex).

https://doi.org/10.1016/j.solmat.2026.114195
Received 12 October 2025; Received in revised form 18 December 2025; Accepted 23 January 2026

ingress and other contaminant-related degradation mechanisms affecting TOPCon solar cells.

Our previous work revealed that glass-backsheet TOPCon modules with different types of POE can experience significant degradation with a reduction in maximum power (P_{max}) ranging from 4%$_{rel}$ to 65%$_{rel}$ after 1000 h of damp heat (DH) testing [5]. This degradation is attributed to electrochemical reactions triggered by moisture ingress, which interacts with cell metallisation, ribbon wires, residual contaminants, soldering flux, and additives released from the POE. These reactions contributed to a considerable increase in series resistance (R_s). These findings highlight the pronounced susceptibility of TOPCon solar cells to humidity-induced and contaminant-induced degradation and also underscore the potential risks associated with certain types of POE. Furthermore, TOPCon solar cells are known to be highly sensitive to specific contaminants, such as acetic acid generated through the hydrolysis of EVA encapsulants [4,19,20], as well as sodium (Na) ions that can be released from the glass during prolonged high-voltage operation [21]. In addition, soldering flux has been identified as a factor contributing to humidity-induced degradation in TOPCon modules [22]; however, it is noteworthy that soldering flux does not appear to affect the cells in the absence of moisture [23]. It is important to note that these earlier investigations were conducted using previous-generation TOPCon cells fabricated without laser-assisted firing technologies. The degradation mechanisms and sensitivity of current TOPCon cells may be different.

Recently, laser-assisted firing, including laser-enhanced contact optimisation (LECO), has been increasingly employed in manufacturing TOPCon solar cells to further enhance the solar cell efficiency [24–26]. Laser-assisted firing techniques reduce the contact resistivity between the semiconductor and metal electrode on both sides of the TOPCon solar cell, while simultaneously improving the surface passivation at lower firing temperatures [26]. A cell-level reliability assessment conducted by Wu et al. from our group demonstrated that laser-enhanced contact firing can significantly enhance the reliability of TOPCon solar cells when exposed to sodium chloride (NaCl), due to the use of aluminium-less or even aluminium-free silver pastes [25]. Furthermore, this study showed that the glass/backsheet module with TOPCon cells fabricated with laser-assisted contact firing exhibited greater stability compared to the module with baseline TOPCon solar cells after 1000 h of DH testing [25]. Despite these promising findings, a notable lack of comprehensive studies remains regarding the reliability of TOPCon cells with laser-assisted fired contacts, particularly when using different bills of materials (BOMs).

The objective of this study is to systematically investigate the impact of the BOM on the DH-induced degradation of TOPCon solar cells fabricated in 2024 using laser-assisted firing processes. We will show that these solar cells exhibit a previously unreported failure mechanism and systematically evaluate the contribution of encapsulation materials to their development.

2. Experimental method

Bifacial n-type TOPCon solar cells (182 mm × 182 mm), fabricated in 2024 using an industrial laser-assisted firing process for contact formation, were employed in this study. The TOPCon cells featured a boron-doped emitter (p^+ emitter), silicon dioxide (SiO_x, unintentionally grown)/aluminium oxide (Al_2O_3)/hydrogenated silicon nitride (SiN_x:H) stack, and a screen-printed H-pattern silver (Ag) grid on the front. At the rear side, there was a SiO_2/phosphorus-doped poly silicon (n^+ poly-Si)/SiN_x:H stack and a screen-printed H-pattern Ag grid. A laser-assisted firing process was applied to the metal contact formation on both sides. Fig. 1 (a) shows the schematic of the final TOPCon solar cell. All cells were soldered on both sides to connect ribbon/tabbing wires to the busbar of cells, forming a 3-cell string. Subsequently, solar cells were encapsulated with various BOMs to construct the module structures depicted in Fig. 1(b). There were two types of commercial EVA (EVA-1 and EVA-2) and two types of POE (POE-1 and POE-2), as well as one type of EPE. EVA-1 is white EVA, containing highly reflective additives such as titanium dioxide (TiO_2), and it is commonly used as a rear-side encapsulant in PV modules to improve light reflectance [27]. EVA-2 is a transparent EVA. The backsheet used in this work was a commercial CPC backsheet. The encapsulation process was carried out at the R&D

(a) Schematic of TOPCon solar cell

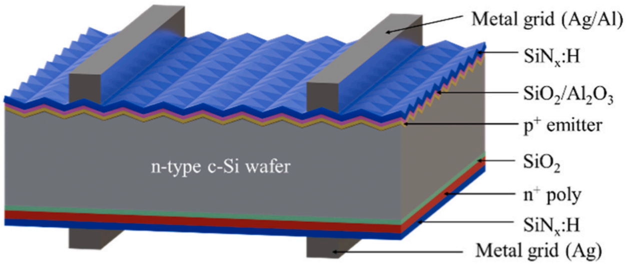

(b) Detail of module structure

ID	Front side	Rear side
M1	Glass/POE-1	POE-1/Backsheet
M2	Glass/POE-2	POE-2/Backsheet
M3	Glass/POE-1	EVA-1/Backsheet
M4	Glass/POE-2	EVA-1/Backsheet
M5	Glass/EPE	EVA-1/Backsheet
M6	Glass/EVA-2	EVA-1/Backsheet

(c) Schematic of module

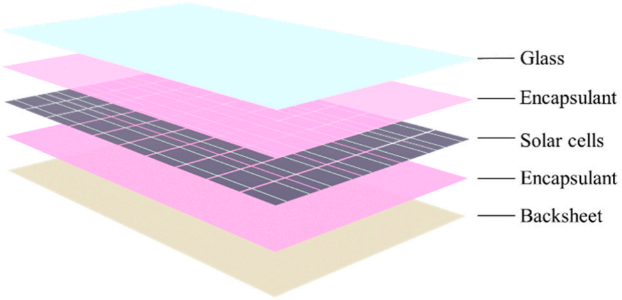

(d) Experimental flow diagram

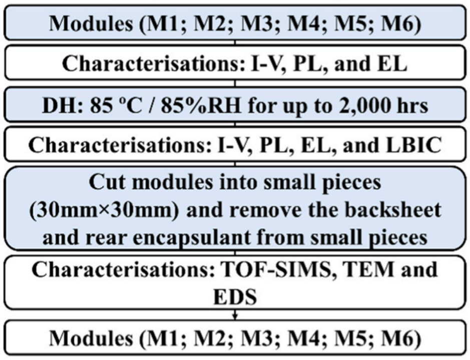

Modules (M1; M2; M3; M4; M5; M6)

Characterisations: I-V, PL, and EL

DH: 85 °C / 85%RH for up to 2,000 hrs

Characterisations: I-V, PL, EL, and LBIC

Cut modules into small pieces (30mm×30mm) and remove the backsheet and rear encapsulant from small pieces

Characterisations: TOF-SIMS, TEM and EDS

Modules (M1; M2; M3; M4; M5; M6)

Fig. 1. (a) Schematic of the TOPCon solar cell. (b) Details of module structures used in this work. (c) Schematic of modules. (d) Experimental flow diagram of this work.

facility of a PV manufacturing site. The mini modules were laminated at 153 °C for 8 min under standard industrial lamination conditions. All mini modules were fabricated explicitly for this study to analyse potential failure issues in this cell technology when exposed to humidity. All modules underwent DH test at 85 °C and 85% RH in an ASLi climate chamber for up to 2000 h to study humidity-induced failures. The current-voltage (I-V) measurements were conducted at standard testing conditions at the initial state and after every 500 h of DH test using a commercial module flash tester (Eternalsun Spire, Spi-Sun SimulatorTM 5600SLP Blue System). Line scan photoluminescence (PL) and electroluminescence (EL) images were captured for all modules by a BT imaging-M1 luminescence line-scan system before and after 1000 h and 2000 h of DH test. PL and EL ratio images were obtained by dividing the PL images captured at the initial state and after 2000 h of DH testing using LumiTools, an advanced image processing software [28]. Light beam-induced current (LBIC) images of selected modules were captured using a LOANA system from pv-tools to identify the location of the failure in solar cells. Subsequently, some aged modules were cut into small pieces (30 mm × 30 mm) using abrasive-waterjet cutting. These tokens were heated on a hot plate at 85 °C to soften the encapsulant. Afterwards, the backsheet and rear-side encapsulant layers (EVA or POE) were carefully removed from these specimens to expose the rear surfaces of the cells. Time-of-Flight Secondary Ion Mass Spectrometer (TOF-SIMS) analysis was conducted on the exposed samples using an ION-TOF SIMS 5 instrument to investigate elemental distributions on the rear surfaces. Positive depth profiles of chemical species were obtained with a 1 keV O_2^+ sputter ion source. Negative depth profiles of chemical species were obtained with a 1 keV C_s^- sputter ion source. In parallel, transmission electron microscopy (TEM) analysis was carried out on selected specimens using a FEI Thermis-Z Double-corrected 60–300 kV S/TEM to examine the microstructural characteristics and integrity of the passivation layers after DH exposure. Energy-dispersive X-ray spectroscopy (EDS) was employed to identify and map the elemental composition within passivation layers. For comparison, fresh, non-encapsulated cells that had not undergone DH testing were also analysed using TOF-SIMS, TEM and EDS to distinguish ageing effects. Additionally, the fresh encapsulants utilised in the modules were characterised by inductively coupled plasma mass spectrometry (ICP-MS) using a NexION 5000 from PerkinElmer to quantify trace elements that may contribute to degradation mechanisms.

3. Results and discussion

3.1. PV module analysis

3.1.1. I-V results

Fig. 2 shows the relative changes in I-V parameters of PV modules before and after DH testing. After 2000 h of DH testing, the P_{max} of the modules decreased by 6%$_{rel}$ – 16%rel, as depicted in Fig. 2 (c). The modules with POE on both sides (M1 and M2) experienced a loss of ~8%$_{rel}$ in P_{max} regardless of the type of POE. However, the two modules with POE on the front side and white EVA on the rear side (M3 and M4) exhibited different performances. The P_{max} of the M3 module (POE-1 and EVA-1) decreased by ~ 13%$_{rel}$, while the M4 module (POE-2 and EVA-1) showed a lower P_{max} loss of ~6%$_{rel}$ after 2000 h of DH testing. The M6 module encapsulated with EVA on both sides degraded ~11%$_{rel}$. The most pronounced degradation, with a P_{max} reduction of ~16%$_{rel}$, was observed in the M5 module with EPE on the front side and white EVA (EVA-1) on the rear side after 2000 h of DH testing. Previous research suggested that the key contributor to humidity-induced degradation on TOPCon cells was an increase in R_s [5,7]. However, the degradation observed in this study was attributed to both a decrease in open-circuit voltage (V_{oc}) by 1%$_{rel}$ – 4%$_{rel}$ [Fig. 2 (a)] and the increase in R_s by 24%$_{rel}$ – 95%$_{rel}$ [Fig. 2 (d)] after 2000 h of DH testing. Notably, the V_{oc} decrease started only after 500 h of DH testing, as shown in Fig. 2 (a). The M3 module with POE-1 on the front side and EVA-1 on the rear side experienced the highest reduction in V_{oc} at ~4%$_{rel}$ after 2000 h of DH testing. Conversely, Fig. 2 (b) illustrates that the short-circuit current density (J_{sc}) of all modules remained relatively stable. This suggests that light absorption and charge carrier generation were not affected; however, it indicates that increased recombination occurs either in the silicon bulk, surface, junction, or interface. An increase in R_s after DH

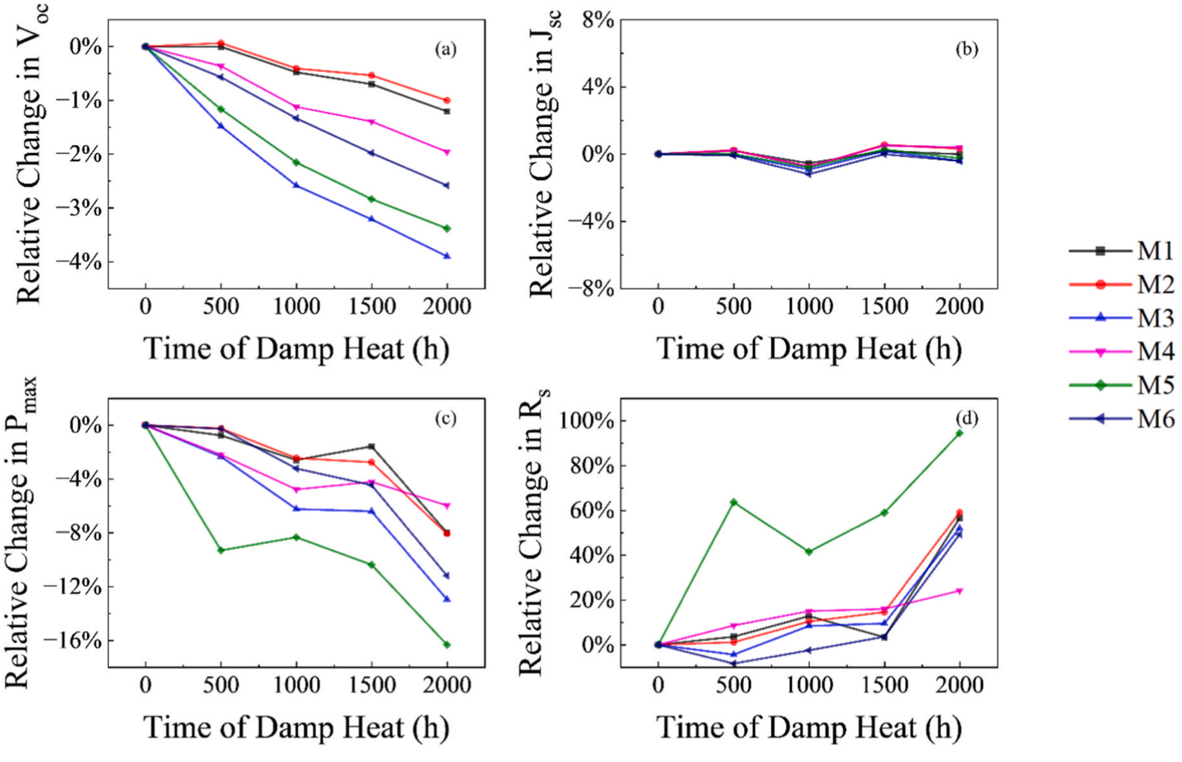

Fig. 2. Relative changes in (a) V_{oc}, (b) J_{sc}, (c) P_{max}, and (d) R_s of modules for up to 2000 h of DH testing.

testing on both module and cell levels (non-encapsulated cell) has been widely observed [5–7,21,29]. This increase is attributed to the corrosion of metal contacts, particularly on the front side of TOPCon solar cells. On the other hand, the degradation of V_{oc} after DH testing or highly accelerated temperature and humidity stress testing (HAST) was mainly observed at the cell level [29,30]. Notably, the decrease in V_{oc} after DH testing at the module level has not been previously reported, making this the first observation of this new failure mode in module-level testing.

3.1.2. PL, EL and LBIC results

Fig. 3 presents the PL and EL images of modules before and after DH testing. A reduction in PL intensity was observed across all modules after DH testing, as shown in Fig. 3 (b), consistent with a corresponding decrease in EL intensity [Fig. 3 (d)]. This suggests increased recombination after DH testing, leading to a reduction in V_{oc} [31]. These results aligned well with the relative changes in I-V parameters shown in Fig. 2. It is worth noting that specific patterns, such as areas highlighted in red circles in Fig. 3 (b), emerged on some solar cells after DH testing. These patterns indicate that degradation was more severe in the central regions of the cells than at the edges, likely due to unintentional AlO_x deposition on the rear surface. In this work, AlO_x is intentionally deposited on the front surface of the TOPCon solar cells to improve surface passivation via its strong negative fixed charge. However, during atomic layer deposition (ALD) the wafers are placed in a reactor in which the reactive gases fill the entire chamber. The precursors (trimethylaluminum and H_2O or O_3) can diffuse around the wafer edges and, if the back-to-back wafer stack is not perfectly sealed, also penetrate the gap between the wafers and reach parts of the rear surface. Any exposed Si or SiO_2 surface with available -OH groups then participates in the self-limiting ALD surface reactions, so Al_2O_3 is conformally deposited not only on the intended front side but also on the wafer edges and localised areas of the rear side. An AlO_x barrier layer was demonstrated previously by our group to mitigate the recombination loss of TOPCon solar cells [32]. The detailed analysis will be discussed in the following sections.

Fig. 4 illustrates the ratio of PL images and EL images for both the M3 and M5 modules. These ratios were calculated by dividing the initial images by the images taken after 1000 h of DH testing, highlighting the areas that exhibit significant degradation. The bright areas indicate a reduction in PL or EL intensity after 1000 h of DH testing. The regions where both PL and EL intensities decreased are marked by the blue circle in Fig. 4 (a) and indicate areas of increased recombination losses. Notably, this recombination region is more pronounced in the PL images [Fig. 4 (a)], whereas it appears slightly distinct in the EL image [Fig. 4

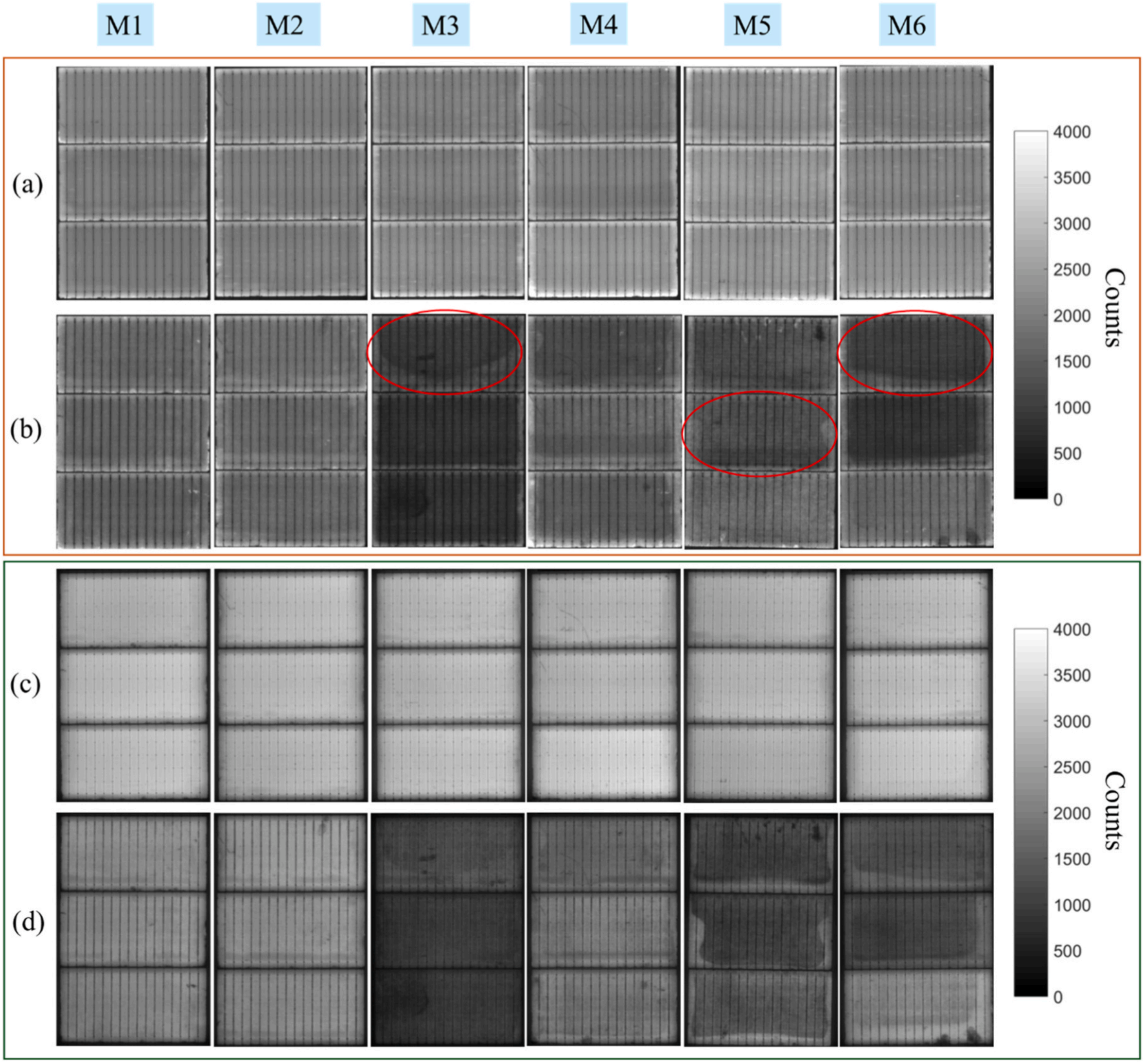

Fig. 3. PL images of all modules (a) before DH testing and (b) after 2000 h of DH testing. EL images of all modules (c) before DH testing and (d) after 2000 h of DH testing.

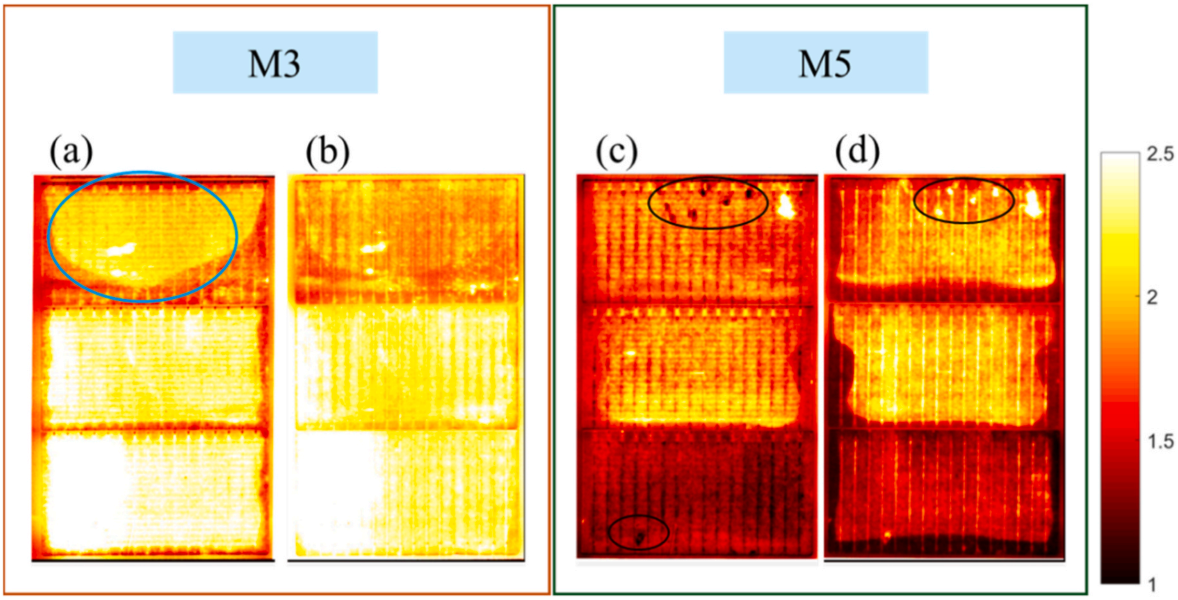

Fig. 4. (a) PL image ratio of the M3 module; (b) EL image ratio of the M3 module; (c) PL image ratio of the M5 module, and (d) EL image ratio of the M5 module. The ratio images were obtained by dividing the EL or PL images taken before DH testing by the image taken after 1000 h of DH testing.

(b)]. Compared to the M5 module, the M3 module exhibited higher recombination losses, resulting in a PL count reduction of approximately a factor of 1.5, observed in all three cells of the M3 module. This finding aligns with the result shown in Fig. 2 (a). In contrast, the recombination losses were not uniformly distributed in the M5 module, with the top and middle cells showing more significant losses than the bottom cells. This variability is likely due to the inherent difference between individual solar cells, even though they originated from the same production line. In addition, localised failures, marked by black circles in Fig. 4 (c) and (d), were observed in the M5 module after DH testing. These failures featured a reduction in EL intensity (high ratio) but an increase in PL intensity (low ratio), suggesting that these localised failures were associated with an increase in R_s (as areas with a high resistance appear brighter in line-scan PL due to restricted carrier transport). Similar shortcomings were also identified in the M1 and M4 modules, as shown in Fig. 3 (b) and (c). The increase in R_s observed in these regions was likely caused by contamination, a phenomenon consistent with our previous findings [5].

Fig. 5 presents the external quantum efficiency (EQE) maps for both the reference module (a fresh module without DH testing) and the M5 module (examined in the middle cell) after 2000 h of DH testing. These images were obtained using LBIC measurements at 405 nm and 940 nm wavelengths. At 405 nm, the light is predominantly absorbed near the front surface, making it highly sensitive to recombination losses at the front surface. In contrast, 940 nm light penetrates deeper into the cell, providing insight into recombination processes occurring in the bulk and/or the rear surface [33]. As shown in Fig. 5 (a), the EQE at both short and long wavelengths for the fresh modules were close to unity, suggesting minimal defects or recombination losses in these modules. In contrast, the EQE at 940 nm for the middle cell of the M5 module is significantly lower than that of the fresh module, exhibiting a similar pattern to the PL images (highlighted by the red circle), as shown in Fig. 5 (b). However, the EQE at 405 nm for the middle cell of the M5 module is similar to that of the fresh module, and no failure pattern similar to the PL images was observed [Fig. 5 (b)]. These findings suggest that the recombination losses causing the reduction in V_{oc} in the M5 module are most likely occurring in the bulk and/or rear side of the cell. It is worth noting that EQE of other modules, such as the M3 module, also exhibit evidence of recombination losses in the bulk and/or rear sides of cells (data not shown).

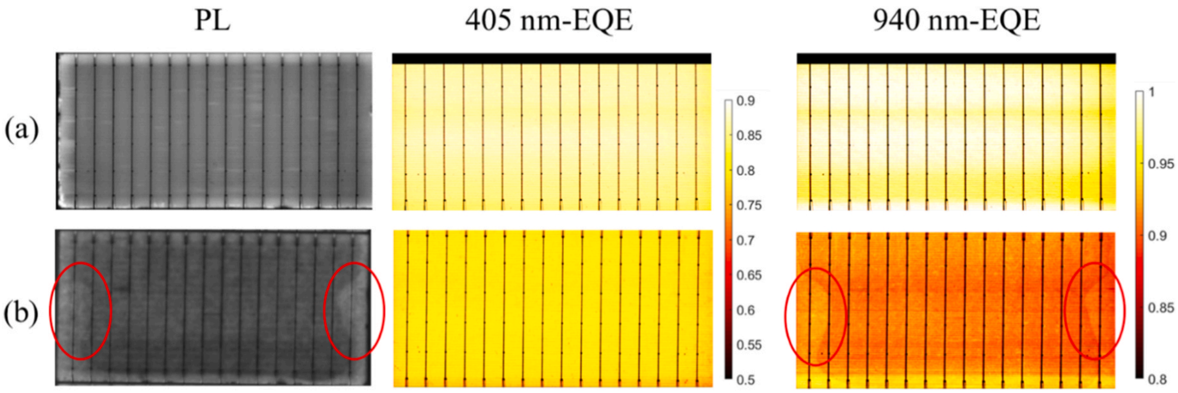

Fig. 5. PL images and EQE maps at 405 nm and 940 nm of (a) the middle cell of the reference module and (b) the middle cell of the M5 module after 2000 h of DH testing. Note that the black regions on the edge of the EQE maps in (a) were due to the measurement artefact.

3.2. Failure mechanism analysis

3.2.1. TOF-SIMS analysis of rear surface of solar cells

TOF-SIMS is a surface-sensitive analytical method employed to detect chemical elements and map their distribution on the surface of solar cells [34]. Fig. 6 shows the positive and negative depth profiles of several elements as a function of sputtering depth at the rear surface of both the fresh cell and the top cell of the M3 module. The sputtering depth was estimated from sputter time and current measured on non-textured samples; therefore, it may not exactly represent the actual depth obtained by TOF-SIMS. The depth scale shown here should be considered as an approximate guide only. It is noted that the fresh cell exhibits patterns similar to those in Fig. 3, which are clearly visible. Compared to regions exhibiting highly degraded patterns (near the centre of the cell), areas with lower degraded patterns (near the edge of the cell) showed significantly higher aluminium (Al) concentrations. This finding provides evidence that unintentional AlO_x deposition occurred at the rear surface of the solar cells during the ALD process conducted on the front surface. Relative to the M3 module [Fig. 6 (c)], the fresh sample had markedly higher Al intensity in the centre of the cell [Fig. 6 (a)], plausibly reflecting batch-to-batch differences between the fresh cells and those in the M3 module, compounded by run-to-run variability in the ALD AlO_x deposition. These unintentional AlO_x layers, situated between the SiN_x and n^+ poly-Si layers, likely acted as barriers, minimising the degradation caused by the contaminant-induced degradation on the rear surface of solar cells after DH testing [32].

Importantly, magnesium (Mg) was detected on the SiN_x layer on the rear surface of the middle cell of the M3 module, as illustrated in Fig. 6 (c) and (d). In contrast, no Mg peaks can be seen in Fig. 6 (a) and (b). Since the TOF-SIMS measurement was captured on the area without the finger/busbar of cells, only non-contact regions were detected by TOF-SIMS. The Mg detected in the M3 module cannot be attributed to metal contacts that might contain Mg [35,36]. Magnesium oxide (MgO) is commonly used in white EVA to neutralise acetic acid produced through hydrolysis [7,27]. Therefore, it is highly plausible that the Mg detected originated from the encapsulant and migrated during DH testing.

Fig. 6 (f) shows a significant oxygen (O) peak ($\sim 5 \times 10^5$) extending approximately 18 nm into the SiN_x layer, whereas the fresh cell in Fig. 6 (e) exhibits a similar O peak confined only to the outermost surface. This suggests that O from the encapsulant or moisture can come into contact with the SiN_x layer, where it likely reacts with Mg, causing corrosion and increasing recombination losses.

In addition to Mg and O, Na was also detected in the SiN_x layer of the M3 module [Fig. 6 (c) and (d)]. However, its intensity was lower than that of Mg and O. It has been reported that Na-based salts can lead to a significant V_{oc} reduction in TOPCon solar cells [21,29,32]. However, Fig. 6 (a) and (b) show that the fresh cell already contained Na between the SiN_x layer and the n^+ poly-Si layer on the rear surface. Solar cells may be contaminated with Na due to improper handling during cell processing [6]. As the fresh cells exhibited no measurable change in V_{oc} following 500 h of DH testing (non-encapsulated cell-level testing, data not shown), whether Na played a role in the recombination losses observed in this study's degraded modules remains inconclusive.

The hydrogen (H^-) depth profiles reveal distinct differences between the fresh and M3 samples, particularly concerning their distribution at the poly-Si/SiO_x interface. In the near-surface region and within the SiN_x layer, both samples exhibit a similar high intensity of H^-. However, within the deeper poly-Si layer, the H^- signal is consistently higher in the M3 module than in the fresh sample, likely caused a chemical reaction occurring under DH conditions. The most notable distinction appears at the poly-Si/SiO_x interface (~150–170 nm depth). The fresh cell displays a distinct peak, indicating an accumulation of hydrogen. This suggests a higher hydrogen concentration at the poly-Si/SiO_x interface or within the silicon oxide layer, passivating defect sites [37,38]. It should be noted that the overall hydrogen signal of the M3 module is significantly higher than that of the fresh sample. It is well known that hydrogen plays a key role in achieving low interface defect density at the c-Si/SiO_x interface, and that excessively high or low hydrogen concentrations can result in an increase in defect density [37].

A separate recovery experiment provides additional support for the involvement of H, which strongly suggests that interfacial H plays a crucial role in the degradation process. When a similar set of degraded minimodules (M4, module with EVA1 on the rear side) underwent dark annealing at 150 °C for 100 h, the V_{oc} recovered by approximately 10 mV (data not shown). This thermal treatment is known to redistribute hydrogen within the cell structure. Previous reports have indicated similar degradation–recovery cycles of poly-Si/SiO_x passivation under dark anneal or illumination, with recovery kinetics driven by the motion of hydrogen [39]. It is important to note that negative-ion SIMS signals for H^- can be influenced by matrix effects (as well as co-sputtered OH^-), so absolute counts should be interpreted with caution between samples [39]. In this context, we primarily rely on the profile shapes and the presence or absence of the interfacial peak, which continue to serve as robust indicators of hydrogen localisation.

3.2.2. TEM and EDS analysis of passivation layers

Fig. 7 presents the TEM images (with and without #Area markers), EDS mapping and corresponding intensity profiles of the non-contact regions on the rear surface of the middle cells of the M3 module and the M2 module, as well as the fresh cell, to confirm the distribution of chemical elements. The regions analysed in the modules were located within highly degraded patterned areas, whereas the region analysed in the fresh cell was situated near the edge of the cell, in an area with less degraded patterns. As shown in Fig. 7 (a), two layers, SiN_x and n^+ poly-Si, were observed in the middle cell of the M3 module. A substantial amount of Mg was detected within the SiN_x layer, with penetration depths reaching approximately 35 nm, indicated in Area #1. This observation is consistent with the TOF-SIMS results. The intensity profile compares the elemental intensities detected in Area #1, Area #2 and Area #3, clearly demonstrating that the Mg signal was confined to Area #1.

Additionally, O was observed in the same region, as evidenced by the EDS maps, suggesting that Mg may be present in the form of MgO. This MgO likely originated from the white EVA used on the module's rear side and diffused into the SiN_x layer. Fig. 7 (b) shows the interfaces in the rear surface of the middle cell of the M2 module encapsulated by POE on both sides, with the analysed area located at the centre of that middle cell. Unlike EVA, POE has acrylates, acrylic acids or n-alkanes instead of the vinyl acetate (VA), thereby precluding the formation of acetic acid during degradation [40,41]. Consequently, POE formulations typically incorporate significantly lower concentrations of MgO [7]. This was confirmed by the fact that only a weak Mg signal was detected, and no significant Mg diffusion into the SiN_x layer was observed, as confirmed by both EDS mappings and the intensity profile [Fig. 7 (b)]. Moreover, no Mg was detected in the fresh cell [Fig. 7 (c)], which is in line with the TOF-SIMS results.

Moreover, Al was observed between the SiN_x layer and the n^+ poly-Si layer in the fresh cell, as demonstrated by EDS mappings and the intensity profile. A strong O signal co-localised with Al suggests the formation of an AlO_x layer between the SiN_x layer and the n^+ poly-Si layer, which may cause the pattern on the rear surface of solar cells. This finding aligns with the TOF-SIMS results. According to the EDS mappings, the AlO_x layer in the fresh cell measured approximately 40 nm. This measured thickness is substantially larger than the typical 10 nm or less reported for intentionally deposited Al_2O_3 passivation layers in TOPCon solar cells [42,43]. Two primary factors may account for this discrepancy. First, the AlO_x layer in our samples is not an intentionally deposited film but is likely an unintentional byproduct of the fabrication process. Consequently, its formation is not subject to the precise thickness controls used for dedicated passivation layers, which could lead to a thicker and more variable film. Second, the measurement technique may

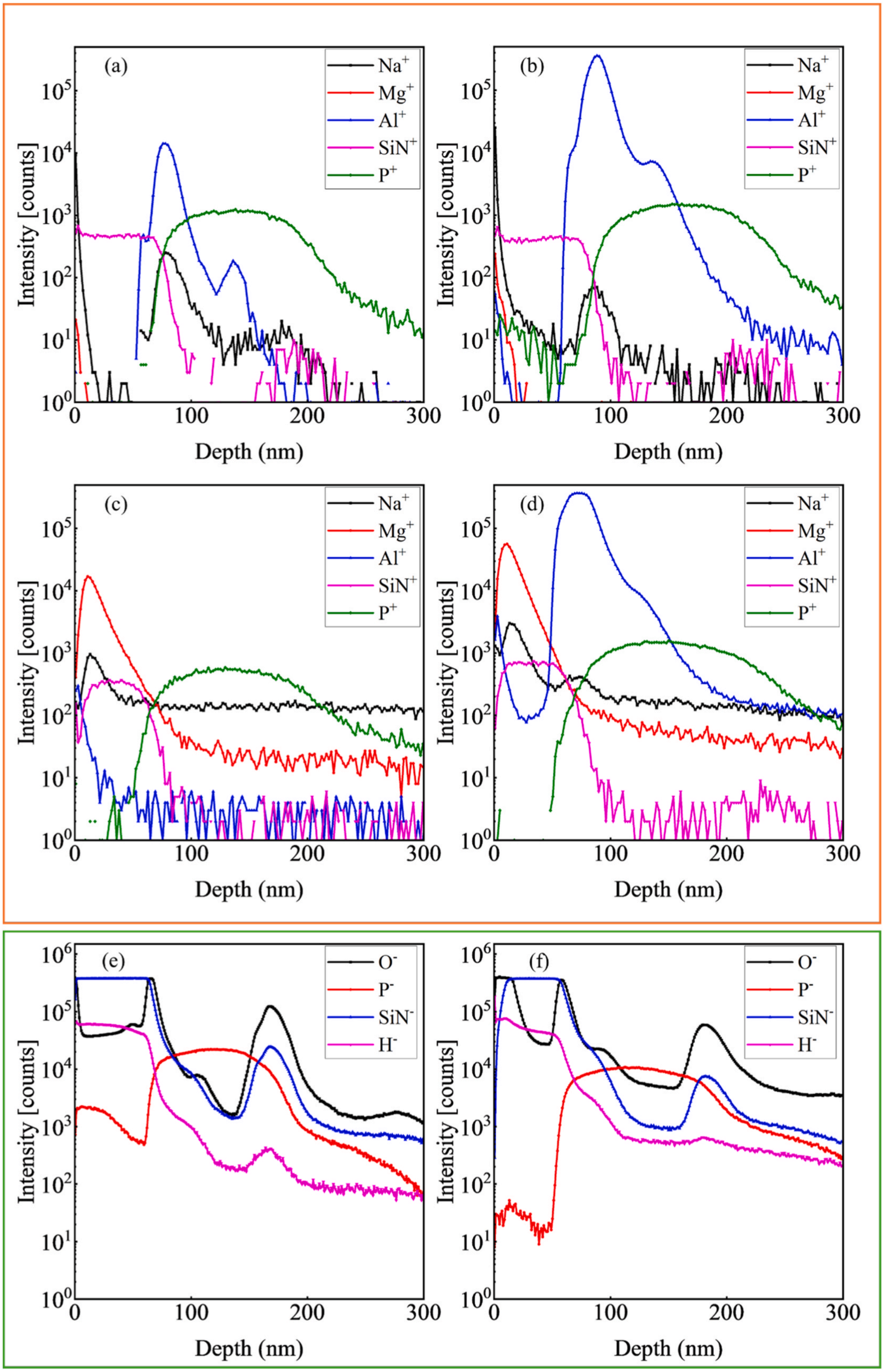

Fig. 6. Positive ion depth profiles of Na, Mg, Al, P, and SiN_x from the rear surface of: (a) the centre region of the fresh cell, corresponding to the highly degraded patterned area observed in the M3 module; (b) the edge region of the fresh cell, resembling the low-degraded, non-patterned area in the M3 module; (c) the top cell of the M3 module within the highly degraded patterned area; and (d) near the edge of the top cell of the M3 module within the low-degraded, non-patterned area. All measurements were conducted exclusively on non-contact regions. Negative ion depth profiles of O, P, SiN_x and H from the rear surface of (e) the centre region of the fresh cell, corresponding to the highly degraded patterned area observed in the M3 module; and (f) the top cell of the M3 module within the highly degraded patterned area.

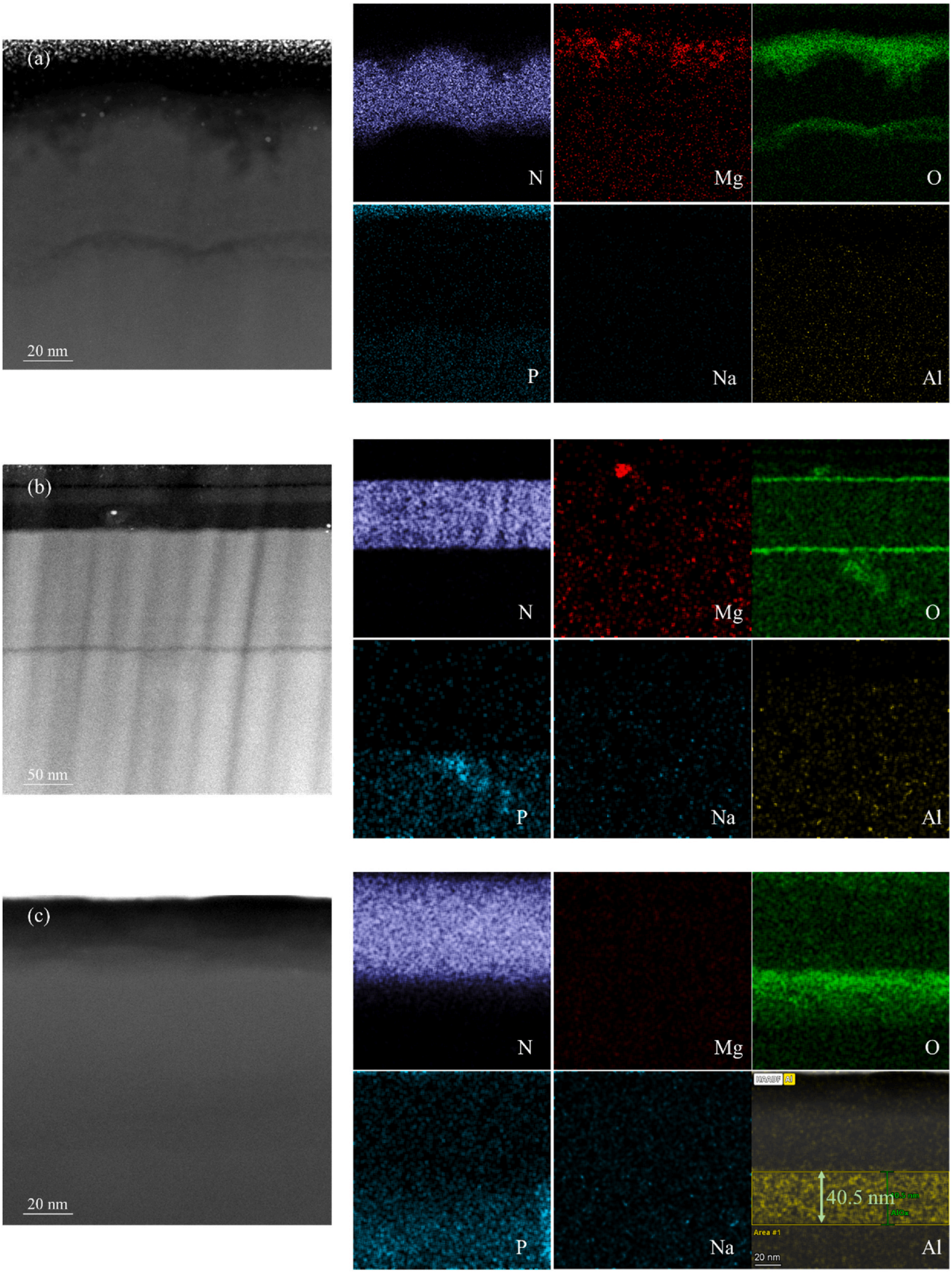

Fig. 7. TEM images (with and without #Area markers) of interfaces without metal contact in the pattern region of (a) the M3 module and (b) the M2 module, and the non-pattern region of the fresh cell. The corresponding EDS mappings show the chemical elements, and the intensity profiles compare the intensity in different areas.

introduce an artefact that exaggerates the layer's thickness. It is well-documented that amorphous AlO_x is susceptible to electron beam-induced radiolysis during TEM analysis, which can reduce it to metallic Al [44]. This newly formed metallic Al can then be induced by the high-energy STEM probe to diffuse into adjacent layers, resulting in an apparent thickening of the aluminium-containing region. Given these considerations, the ~40 nm thickness observed via TEM may not accurately represent the actual dimensions of the layer in the

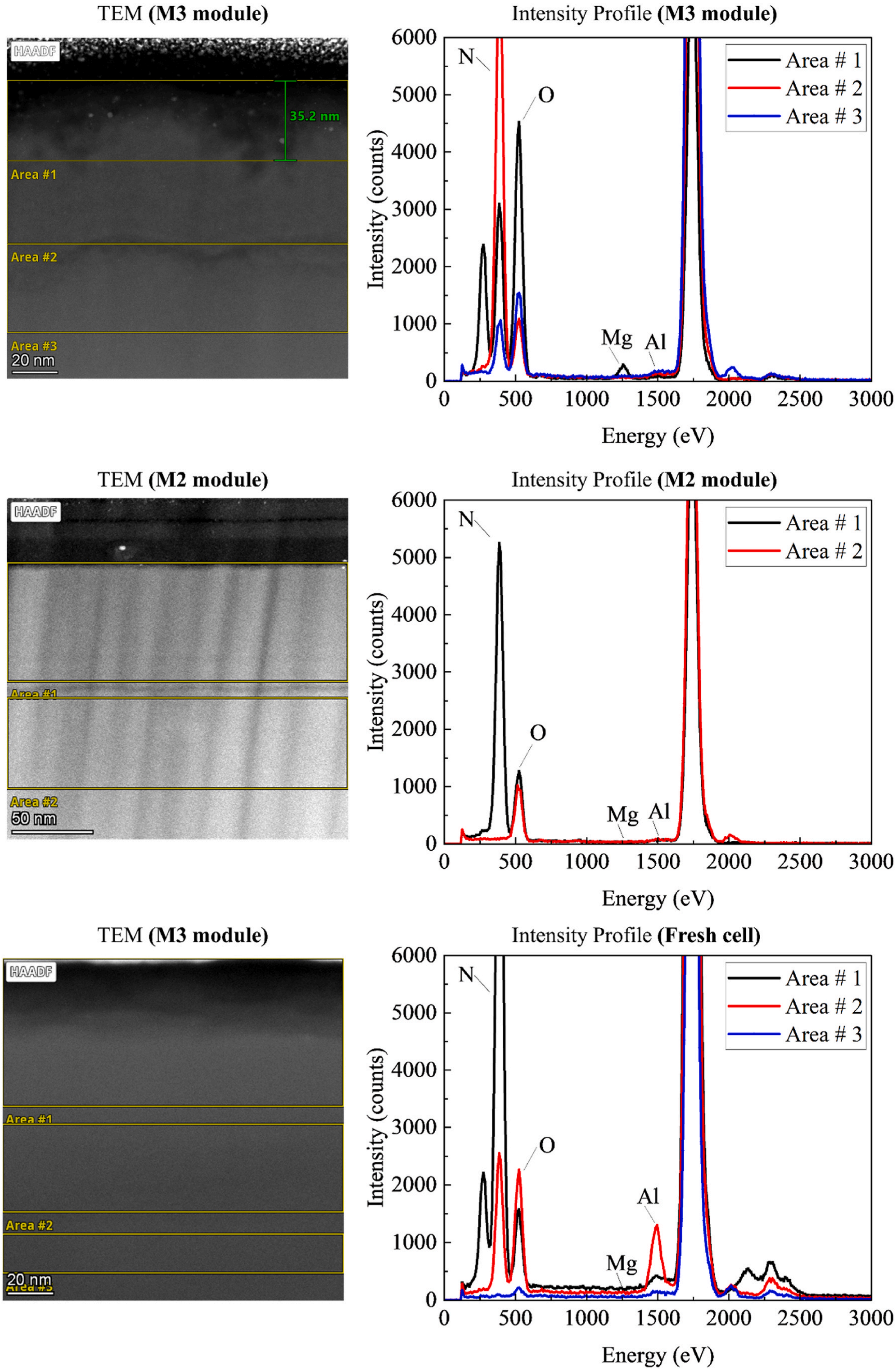

Fig. 7. (*continued*).

as-fabricated device. Further characterisation using techniques less prone to beam damage is necessary to validate this observation.

3.2.3. *ICP-MS analysis of encapsulant*

ICP-MS was employed to analyse the fresh encapsulant used in the modules to identify the source of Mg detected in TEM and TOF-SIMS results. The results are summarised in Table 1. Notably, the EVA encapsulants have the highest concentration of Mg, with the white EVA (EVA-1) showing particularly elevated levels, consistent with findings reported in previous studies [7]. Among the tested materials, POE-1 contained the lowest Mg concentration, at 0.5 ppm, whereas POE-2 contained 193 ppm, which is higher than that measured for EVA-2. Nevertheless, the modules encapsulated by either POE-1 or POE-2 on both sides demonstrated comparable performances after DH testing, as indicated in Fig. 2, implying that Mg may be minimally released from POE under DH conditions. In addition to Mg, Na and calcium (Ca) were also detected across all encapsulants (Table 1). However, the concentrations of Na and Ca were considerably lower than those of Mg. Except for EVA-1, the levels of Na and Ca were comparable across the different encapsulants. Despite this similarity, the extent of power degradation in the corresponding modules varied markedly, ranging from 6%$_{rel}$ to 16%$_{rel,}$ depending on the encapsulant used. This suggests that Na and Ca are unlikely to be the primary contributors to the observed degradation. In summary, these results suggest that the elevated Mg content detected in the white EVA was likely the source of the Mg-induced recombination loss observed in the solar cells during DH testing. By contrast, Mg appears to remain relatively stable in the other encapsulant materials, resulting in a negligible contribution to degradation under the tested conditions.

3.2.4. *Hypothesised failure mechanism*

The combined I-V, PL/EL, EQE and micro-analytical evidence (TOF-SIMS, TEM-EDS, ICP-MS) indicates that a rise in rear-side recombination drives the damp-heat-induced loss of V_{oc} in these TOPCon modules. Electrically, the I-V data show a pronounced V_{oc} reduction with only minor changes in J_{sc} and fill factor trends, inconsistent with a dominant series-resistance failure. PL images reveal an uniform baseline drop with superimposed local dark features after DH exposure, hallmarks of increased recombination rather than transport limitations. Spectrally, the EQE response degrades most at long wavelengths, where photogeneration occurs deeper in the wafer and carrier collection is most sensitive to rear-surface recombination, reinforcing a rear-limited mechanism.

Mechanistically, we attribute the degradation to Mg-bearing species released from the encapsulant—particularly white EVA—that hydrate under 85 °C/85 % RH to create an alkaline micro-environment via Eq. (1) [45,46]. This alkaline environment has been shown to accelerate SiN_x oxidation [Eq. (2)] [47–49].

$$MgO + H_2O \rightarrow Mg^{2+} + 2OH^{-} \leftrightarrow Mg(OH)_2 \tag{1}$$

$$Si_3N_4 + 6H_2O \rightarrow 3SiO_2 + 4NH_3 \tag{2}$$

This reaction pathway is consistent with (i) ICP-MS/TOF-SIMS detection of Mg at the rear stack, (ii) TOF-SIMS depth profiles showing co-enrichment of Mg and O within the SiN_x: H layer (penetration on the order of a few × 10 nm), and (iii) TEM-EDS cross-sections that reveal a speckled, porous band (~35 nm) at the SiN_x layer surface after DH testing. Additionally, the Mg → $Mg(OH)_2$ conversion is intrinsically volume-expansive, which promotes micro-voiding and mechanical damage in the already-stressed SiN_x layer, further opening diffusion pathways for water and O [50].

Once the SiN_x layer integrity is compromised, moisture may permeate the poly-Si contact along grain boundaries, as indicated by the higher H and O concentration observed in the M3 module compared with the fresh cell [Fig. 6 (e–f)] [51,52]. However, the poly-Si layer's oxidation was not observed in the TEM image of the M3 module [Fig. 7 (a)]. Further work is ongoing to determine the underlying reaction between moisture and the poly-Si layer under DH conditions. The increased interfacial hydrogen after DH testing may depassivate $Si - H$ bonds at the SiO_x/c-Si interface and create H_2 at the interface [53–56]. The depassivation could increase recombination at the interface.

In addition, the local structural damage may also intensify the problem; bright, high-contrast spots observed in TEM at Mg-rich locations [Fig. 7 (a)] are consistent with micro-pinhole-like defects within the passivation stack [57,58]. Such defects likely act as high-recombination shunts, locally short-circuiting the passivation and creating hotspots of emitter–base coupling [59,60]. The coexistence of distributed chemical depassivation (raising the average recombination) and discrete pinhole sites (creating local spikes) explains the mixed “global-plus-speckled” appearance of the post-DH luminescence maps.

Taken together, SiN_x layer corrosion, depassivation of interface dangling bonds, and pinhole formation could increase the rear saturation current $J_{0,\ rear}$, thereby reducing V_{oc} [61]. This causal chain aligns with the electrical signatures (I-V/EQE), the spatial recombination fingerprints (PL/EL), and the compositional/structural diagnostics (TOF-SIMS, TEM-EDS, ICP-MS) measured on the same devices.

4. Conclusion

This work investigates the impact of DH on the performance of glass/backsheet modules incorporating bifacial n-type TOPCon with laser-assisted fired contacts, encapsulated with various BOMs, including EVA, POE and EPE. The modules experienced a degradation in P_{max} ranging from 6%$_{rel}$ to 16%$_{rel}$ after 2000 h of DH testing. Modules encapsulated with POE on both sides degraded by ~8%$_{rel}$, regardless of the type of POE used. In contrast, modules utilising POEs on the front side and the white EVA on the rear side showed varying degradation levels: the module with POE-1 exhibited a more substantial P_{max} loss of ~13%$_{rel}$, whereas the module with POE-2 degraded by ~6%$_{rel}$ after 2000 h of DH testing. The most significant degradation, ~16%$_{rel}$, was observed in the module encapsulated with EPE on the front side and the white EVA on the rear side. Notably, there was no consistent trend in degradation behaviour associated with different encapsulant types on the front side. However, it can be concluded that the modules with POE on the rear side showed relatively greater stability compared to those with white EVA on the rear side. It is noteworthy that the primary driver of the degradation was a reduction in V_{oc} rather than the increased R_s after DH testing, which diverges from previous findings that predominantly attributed DH-induced degradation to metallisation corrosion. PL and EQE measurements at short and long wavelengths revealed recombination loss patterns, primarily occurring in the bulk and/or on the rear side of TOPCon solar cells. Supporting this, TOF-SIMS and TEM analyses indicated that these recombination losses were associated with the presence of Mg and O in the SiN_x layer. ICP-MS results revealed that the white EVA contained the highest Mg concentration among the encapsulants examined.

This finding elucidates the pronounced increased degradation noted in modules featuring white EVA on the rear side. The presence of Mg-bearing species in the white EVA hydrates at 85 °C and 85% RH can lead to an alkaline micro-environment that accelerates the corrosion of the SiN_x: H layer. Moisture may penetrate the poly-Si layer along grain boundaries, but further work is needed to confirm this. Depassivation of the dangling bonds likely occurs at the SiO_x/c-Si interface due to the increased interfacial H concentration under DH conditions. Localised

Table 1

ICP-MS results of all types of encapsulants used in this work.

	POE-1	POE-2	EVA-1	EVA-2	EPE
mg (ppm)	0.50	1.9×10^2	1.8×10^3	1.8×10^2	95
Na (ppm)	1.5	1.7	48	1.6	0.90
Ca (ppm)	16	19	20	17	13

pinhole-like defects at Mg-rich sites function as recombination shunts; when combined with depassivation, this phenomenon elevates $J_{0,\ rear}$, and diminishes V_{oc}.

This study reports a Mg-related degradation behaviour in silicon PV modules under DH conditions, specifically highlighting the role of MgO in inducing unexpected recombination-related performance losses in TOPCon modules. While the presence of Mg in white EVA encapsulants and its influence on acetic acid-induced degradation have been reported previously, the impact of MgO on performance degradation in TOPCon module has not been explicitly addressed. The resulting mechanistic insights informed targeted optimisation of the cell architecture and encapsulant, including Mg control in white EVA; these measures have been incorporated upstream of module manufacture and have materially reduced the susceptibility observed in commercial-scale products. This work aims to support the broader PV community in improving module reliability. At the same time, further validation across different manufacturing facilities will help confirm the mechanism and accelerate wider adoption of reliability improvements.

CRediT authorship contribution statement

Haoran Wang: Writing – original draft, Visualization, Validation, Methodology, Investigation, Formal analysis, Data curation, Conceptualization. **Chandany Sen:** Writing – review & editing, Supervision, Methodology, Investigation, Formal analysis. **Muhammad Umair Khan:** Methodology, Investigation. **Ting Huang:** Visualization, Resources, Conceptualization. **Hao Song:** Visualization, Resources, Conceptualization. **Munan Gao:** Visualization, Resources, Conceptualization. **Ruirui Lv:** Visualization, Resources, Conceptualization. **Yuanjie Yu:** Visualization, Resources, Conceptualization. **Bram Hoex:** Writing – review & editing, Supervision, Resources, Project administration, Funding acquisition, Conceptualization.

Declaration of competing interest

The authors declare that they have no known competing financial interests or personal relationships that could have appeared to influence the work reported in this paper.

Acknowledgement

This work was supported by the Australian Government through the Australian Centre for Advanced Photovoltaics (ACAP), also funded by ARENA. The responsibility for the views, information, or advice expressed herein is not accepted by the Australian Government. The authors appreciate the support provided by the Australian Government's Trailblazer for Recycling & Clean Energy program, led by UNSW & the University of Newcastle. The authors acknowledge the use of the ION-TOF SIMS 5, FEI Thermis-Z Double-corrected 60–300 kV S/TEM, TESCAN AMBER X 2 Plasma FIB-SEM and ICP-MS NEXION5000, as well as the scientific and technical guidance provided by Dr Bill Bin Gong, Dr Songyan Yin and Ms Khorshed Chinu from UNSW Mark Wainwright Analytical Centre, as well as Dr Felix Theska and Dr Jiangtao Qu from USYD Sydney Microscopy & Microanalysis. The authors extend their gratitude to the SLDOT team at SPREE UNSW, both at TETB and SIRF, for their invaluable support in upholding health and safety standards within the lab and ensuring the seamless operation of the facility, which facilitated the progress of our work.

Data availability

Data will be made available on request.

References

[1] International Technology Roadmap for Photovoltaic, vol. 16, ITRPV, 2025. Available: https://www.vdma.eu/en-GB/international-technology-roadmap-photovoltaic.

[2] I.M. Peters, J. Hauch, C. Brabec, P. Sinha, The value of stability in photovoltaics, Joule 5 (12) (Dec. 2021) 3137–3153, https://doi.org/10.1016/j.joule.2021.10.019.

[3] X. Wu, et al., Is TOPCon ready for EVA? Insights from damp heat testing of glass-backsheet modules, Sol. Energy Mater. Sol. Cell. 288 (Aug. 2025) 113650, https://doi.org/10.1016/j.solmat.2025.113650.

[4] P.M. Sommeling, J. Liu, J.M. Kroon, Corrosion effects in bifacial crystalline silicon PV modules; interactions between metallization and encapsulation, Sol. Energy Mater. Sol. Cell. 256 (Jul. 2023) 112321, https://doi.org/10.1016/j.solmat.2023.112321.

[5] C. Sen, et al., Buyer aware: three new failure modes in TOPCon modules absent from PERC technology, Sol. Energy Mater. Sol. Cell. 272 (Aug. 2024) 112877, https://doi.org/10.1016/j.solmat.2024.112877.

[6] C. Sen, et al., Hidden traces: insights into how solar cell handling drives damp-heat failures in HJT and TOPCon modules, Sol. Energy Mater. Sol. Cell. 289 (Aug. 2025), https://doi.org/10.1016/j.solmat.2025.113695.

[7] Y. Ye, et al., Damp-heat stability investigation of glass-backsheet modules based on TOPCon solar cells, Sol. Energy Mater. Sol. Cell. 292 (Oct. 2025), https://doi.org/10.1016/j.solmat.2025.113764.

[8] C. Sen, et al., Four failure modes in silicon heterojunction glass-backsheet modules, Sol. Energy Mater. Sol. Cell. 257 (Aug. 2023) 112358, https://doi.org/10.1016/j.solmat.2023.112358.

[9] J. Karas, et al., Damp heat induced degradation of silicon heterojunction solar cells with Cu-Plated contacts, IEEE J. Photovoltaics 10 (1) (Jan. 2020) 153–158, https://doi.org/10.1109/JPHOTOV.2019.2941693.

[10] Y. Bai, et al., Lower levelized cost of energy achievement of silicon heterojunction solar modules with low water vapor transmission rate encapsulants, Energy Technol. 11 (7) (Jul. 2023), https://doi.org/10.1002/ente.202201466.

[11] Ch Hirschl, et al., Determining the degree of crosslinking of ethylene vinyl acetate photovoltaic module encapsulants—A comparative study, Sol. Energy Mater. Sol. Cell. 116 (Sep. 2013) 203–218, https://doi.org/10.1016/j.solmat.2013.04.022.

[12] A. Dhaundiyal, D. Atsu, Energy assessment of photovoltaic modules, Sol. Energy 218 (Apr. 2021) 337–345, https://doi.org/10.1016/j.solener.2021.02.055.

[13] S. Jonai, K. Hara, Y. Tsutsui, H. Nakahama, A. Masuda, Relationship between cross-linking conditions of ethylene vinyl acetate and potential induced degradation for crystalline silicon photovoltaic modules, Jpn. J. Appl. Phys. 54 (8S1) (Aug. 2015) 08KG01, https://doi.org/10.7567/JJAP.54.08KG01.

[14] RenewSys India, “EVA v/s POE: a comparative study of solar panel encapsulants,” RenewSys World. Accessed: December. 15, 2025. [Online]. Available: https://www.renewsysworld.com/post/eva-v-s-poe-a-comparative-study-of-solar-panel-encapsulants.

[15] Z. Yang, et al., Novel EPE co-extruded encapsulating films with UV down-conversion power gain effect for highly efficient solar cells, Sol. Energy Mater. Sol. Cell. 257 (Aug. 2023) 112373, https://doi.org/10.1016/j.solmat.2023.112373.

[16] K. Liu, D.C. Miller, N. Bosco, R.H. Dauskardt, Determining the crosslinking and degradation reaction kinetics in photovoltaic encapsulants using accelerated aging, in: 2024 IEEE 52nd Photovoltaic Specialist Conference (PVSC), IEEE, Jun. 2024, pp. 909–914, https://doi.org/10.1109/PVSC57443.2024.10749611.

[17] J.P. Singh, S. Guo, I.M. Peters, A.G. Aberle, T.M. Walsh, Comparison of glass/glass and glass/backsheet PV modules using bifacial silicon solar cells, IEEE J. Photovoltaics 5 (3) (May 2015) 783–791, https://doi.org/10.1109/JPHOTOV.2015.2405756.

[18] M. Hutchins, The weekend read: bifacial drives PV encapsulant switch, pv magazine (Mar. 20, 2021).

[19] N. Iqbal, et al., Impact of acetic acid exposure on the screen-printed tellurite-based silver contacts, in: Conference Record of the IEEE Photovoltaic Specialists Conference, Institute of Electrical and Electronics Engineers Inc., Jun. 2021, pp. 382–386, https://doi.org/10.1109/PVSC43889.2021.9518870.

[20] A. Kraft, et al., Investigation of acetic acid corrosion impact on printed solar cell contacts, IEEE J. Photovoltaics 5 (3) (May 2015) 736–743, https://doi.org/10.1109/JPHOTOV.2015.2395146.

[21] C. Sen, et al., Accelerated damp-heat testing at the cell-level of bifacial silicon HJT, PERC and TOPCon solar cells using sodium chloride, Sol. Energy Mater. Sol. Cell. 262 (Oct. 2023), https://doi.org/10.1016/j.solmat.2023.112554.

[22] J. Fu, et al., Assessing the impact of solder flux-induced corrosion on TOPCon solar cells, Sol. Energy Mater. Sol. Cell. 294 (Jan. 2026) 113890, https://doi.org/10.1016/j.solmat.2025.113890.

[23] H. Wang, et al., The influence of soldering flux on stability of heterojunction and TOPCon solar cells, Prog. Photovoltaics Res. Appl. (2025), https://doi.org/10.1002/pip.3896.

[24] Q. Wang, K. Guo, S. Gu, W. Huang, W. Wu, J. Ding, Investigation on effects of the laser-enhanced contact optimization process with Ag paste in a boron emitter for n-TOPCon solar cell, Prog. Photovoltaics Res. Appl. (Feb. 2024), https://doi.org/10.1002/pip.3854.

[25] X. Wu, et al., Enhancing the reliability of TOPCon technology by laser-enhanced contact firing, Sol. Energy Mater. Sol. Cell. 271 (Jul) (2024), https://doi.org/10.1016/j.solmat.2024.112846.

[26] T. Fellmeth, et al., Laser-enhanced contact optimization on iTOPCon solar cells, Prog. Photovoltaics Res. Appl. 30 (12) (Dec. 2022) 1393–1399, https://doi.org/10.1002/pip.3598.

[27] Y. ChenLi, et al., Degradation mechanism of TOPCon solar cells in an ambient acid environment, ACS Appl. Mater. Interfaces (Feb. 2025), https://doi.org/10.1021/acsami.4c21774.

[28] D.N.R. Payne, C. Vargas, Z. Hameiri, S.R. Wenham, D.M. Bagnall, An advanced software suite for the processing and analysis of silicon luminescence images, Comput. Phys. Commun. 215 (Jun. 2017) 223–234, https://doi.org/10.1016/j.cpc.2017.02.012.

[29] X. Wu, et al., Unveiling the origin of metal contact failures in TOPCon solar cells through accelerated damp-heat testing, Sol. Energy Mater. Sol. Cell. 278 (Dec. 2024) 113188, https://doi.org/10.1016/j.solmat.2024.113188.

[30] Z. Li, et al., Effect of firing temperature on damp heat stability of n-TOPCon solar cells' rear side, Sol. RRL (Jul. 2025), https://doi.org/10.1002/solr.202500299.

[31] Z. Iskra, M.K. Juhl, J.W. Weber, J. Wong, T. Trupke, Detection of finger interruptions in silicon solar cells using line scan photoluminescence imaging, IEEE J. Photovoltaics 7 (6) (Nov. 2017) 1496–1502, https://doi.org/10.1109/JPHOTOV.2017.2732220.

[32] H. Tong, et al., Mitigating contaminant-induced surface degradation in TOPCon solar cells: mechanisms, impacts, and mitigation, Sol. Energy Mater. Sol. Cell. 286 (Jul. 2025) 113558, https://doi.org/10.1016/j.solmat.2025.113558.

[33] J. Vanek, K. Jandova, R. Barinka, Projection of solar cell back side contact to the LBIC image [Online]. Available: http://www.feec.vutbr.cz, Sep. 2007.

[34] J.C. Vickerman, ToF-SIMS—An overview, in: ToF-SIMS: Surface Analysis by Mass Spectrometry, 2001, pp. 1–40.

[35] Y. Wan, et al., Conductive and stable magnesium oxide electron-selective contacts for efficient silicon solar cells, Adv. Energy Mater. 7 (5) (Mar. 2017), https://doi.org/10.1002/aenm.201601863.

[36] Z. Yao, et al., High-performance and stable dopant-free silicon solar cells with magnesium acetylacetonate electron-selective contacts, Phys. Status Solidi Rapid Res. Lett. 14 (6) (Jun. 2020), https://doi.org/10.1002/pssr.202000103.

[37] C. Hollemann, et al., Changes in hydrogen concentration and defect state density at the poly-Si/SiO$_x$/c-Si interface due to firing, Sol. Energy Mater. Sol. Cell. 231 (Oct. 2021) 111297, https://doi.org/10.1016/j.solmat.2021.111297.

[38] M. Schnabel, et al., Hydrogen passivation of poly-Si/SiO$_x$ contacts for Si solar cells using Al$_2$O$_3$ studied with deuterium, Appl. Phys. Lett. 112 (20) (May 2018), https://doi.org/10.1063/1.5031118.

[39] A.R. Ratnapagol, W. Nemeth, P. Stradins, S. Agarwal, D.L. Young, Degradation and accelerated recovery of surface passivation in n^+, p^+, and intrinsic *poly* -Si/SiO$_x$ passivating contacts for silicon solar cells, Sol. RRL 9 (14) (Jul. 2025), https://doi.org/10.1002/solr.202500133.

[40] G. Oreski, B. Ottersböck, A. Omazic, Degradation processes and mechanisms of encapsulants, in: Durability and Reliability of Polymers and Other Materials in Photovoltaic Modules, Elsevier, 2019, pp. 135–152, https://doi.org/10.1016/B978-0-12-811545-9.00006-9.

[41] G. Oreski, et al., Properties and degradation behaviour of polyolefin encapsulants for photovoltaic modules, Prog. Photovoltaics Res. Appl. 28 (12) (Dec. 2020) 1277–1288, https://doi.org/10.1002/pip.3323.

[42] L. Lu, et al., Dopant diffusion through ultrathin AlO$_x$ and AlO$_x$/SiO$_x$ tunnel layer in TOPCon structure and its impact on the passivation quality on c-Si solar cells, Sol. Energy Mater. Sol. Cell. 223 (May 2021) 110970, https://doi.org/10.1016/j.solmat.2021.110970.

[43] A. Richter, et al., Design rules for high-efficiency both-sides-contacted silicon solar cells with balanced charge carrier transport and recombination losses, Nat. Energy 6 (4) (Apr. 2021) 429–438, https://doi.org/10.1038/s41560-021-00805-w.

[44] G. Noircler, F. Lebreton, E. Drahi, P. de Coux, B. Warot-Fonrose, STEM-EELS investigation of c-Si/a-AlO interface for solar cell applications, Micron 145 (Jun. 2021) 103032, https://doi.org/10.1016/j.micron.2021.103032.

[45] Z. Li, et al., Characterization of reaction products and reaction process of MgO–SiO$_2$–H$_2$O system at room temperature, Constr. Build. Mater. 61 (Jun. 2014) 252–259, https://doi.org/10.1016/j.conbuildmat.2014.03.004.

[46] M. Pettauer, A. Baldermann, S. Eder, M. Dietzel, Hydration of MgO: reaction kinetics and pH control on brucite crystal morphology, Cryst. Growth Des. 24 (7) (Apr. 2024) 3085–3092, https://doi.org/10.1021/acs.cgd.4c00243.

[47] C. Zhang, M. Wu, P. Wang, M. Jian, J. Zhang, L. Yang, Stability of SiN$_x$ prepared by plasma-enhanced chemical vapor deposition at low temperature, Nanomaterials 11 (12) (Dec. 2021) 3363, https://doi.org/10.3390/nano11123363.

[48] H. Lin, et al., Moisture-resistant properties of SiN$_x$ films prepared by PECVD, Thin Solid Films 333 (1–2) (Nov. 1998) 71–76, https://doi.org/10.1016/S0040-6090(98)00812-8.

[49] M. Herrmann, Corrosion of silicon nitride materials in aqueous solutions, J. Am. Ceram. Soc. 96 (10) (Oct. 2013) 3009–3022, https://doi.org/10.1111/jace.12509.

[50] N.T. Luong, M. Holmboe, J.-F. Boily, MgO nanocube hydroxylation by nanometric water films, Nanoscale 15 (24) (2023) 10286–10294, https://doi.org/10.1039/D2NR07140A.

[51] T. Kamiya, Z.A.K. Durrani, H. Ahmed, Control of grain-boundary tunneling barriers in polycrystalline silicon, Appl. Phys. Lett. 81 (13) (Sep. 2002) 2388–2390, https://doi.org/10.1063/1.1509853.

[52] Y. Furuta, et al., Characterization of tunnel barriers in polycrystalline silicon point-contact single-electron transistors, Jpn. J. Appl. Phys. 41 (Part 1) (Apr. 2002) 2675–2678, https://doi.org/10.1143/JJAP.41.2675, 4B.

[53] K.R. McIntosh, X. Dai, Damp-heat degradation and repair of oxide-passivated silicon, Physica Status Solidi (A) Applications and Materials Science 208 (8) (Aug. 2011) 1931–1936, https://doi.org/10.1002/pssa.201026492.

[54] G. Dingemans, W. Beyer, M.C.M. van de Sanden, W.M.M. Kessels, Hydrogen induced passivation of Si interfaces by Al2O3 films and SiO2/Al2O3 stacks, Appl. Phys. Lett. 97 (15) (Oct. 2010), https://doi.org/10.1063/1.3497014.

[55] K.L. Brower, Kinetics of H$_2$ passivation of Pb centers at the (111) Si-SiO$_2$ interface, Phys. Rev. B 38 (14) (Nov. 1988) 9657–9666, https://doi.org/10.1103/PhysRevB.38.9657.

[56] L. Tsetseris, S.T. Pantelides, Migration, incorporation, and passivation reactions of molecular hydrogen at the Si-SiO$_2$ interface, Phys. Rev. B 70 (24) (Dec. 2004) 245320, https://doi.org/10.1103/PhysRevB.70.245320.

[57] A.S. Kale, et al., Understanding the charge transport mechanisms through ultrathin SiO$_x$ layers in passivated contacts for high-efficiency silicon solar cells, Appl. Phys. Lett. 114 (8) (Feb. 2019), https://doi.org/10.1063/1.5081832.

[58] C.L. Anderson, et al., Understanding SiO$_x$ Layer Breakup in poly-Si/SiO$_x$ Passivating Contacts for Si Solar Cells Using Precisely Engineered Surface Textures, ACS Appl. Energy Mater. 5 (3) (Mar. 2022) 3043–3051, https://doi.org/10.1021/acsaem.1c03676.

[59] S. Sadhukhan, et al., Detailed study on the role of nature and distribution of pinholes and oxide layer on the performance of tunnel oxide passivated contact (TOPCon) solar cell, IEEE Trans. Electron. Dev. 69 (10) (Oct. 2022) 5618–5623, https://doi.org/10.1109/TED.2022.3196327.

[60] Z. Yang, et al., Charge-carrier dynamics for silicon oxide tunneling junctions mediated by local pinholes, Cell Rep. Phys. Sci. 2 (12) (Dec. 2021) 100667, https://doi.org/10.1016/j.xcrp.2021.100667.

[61] M.A. Green, Solar Cells: Operating Principles, Technology, and System Applications, Prentice-Hall, Englewood Cliffs, NJ, 1982.